Combining ultrahigh index with exceptional nonlinearity in resonant transition metal dichalcogenide nanodisks

nature photonics

Article

https://doi.org/10.1038/s41566-024-01444-9

Combining ultrahigh index with exceptional nonlinearity in resonant transition metal dichalcogenide nanodisks

Received: 4 August 2023

Accepted: 15 April 2024

Published online: 13 June 2024

Check for updates

George Zograf[1] ✉, Alexander Yu. Polyakov[1], Maria Bancerek[2], Tomasz J. Antosiewicz[1,2], Betül Küçüköz[1] & Timur O. Shegai[1] ✉

Second-order nonlinearity in solids gives rise to a plethora of unique physical phenomena ranging from piezoelectricity and optical rectification to optical parametric amplification, spontaneous parametric down-conversion and the generation of entangled photon pairs. Monolayer transition metal dichalcogenides, such as MoS_2, exhibit one of the highest known second-order nonlinear coefficients. However, the monolayer nature of these materials prevents the fabrication of resonant objects exclusively from the material itself, necessitating the use of external structures to achieve the optical enhancement of nonlinear processes. Here we exploit the 3R phase of a molybdenum disulfide multilayer for resonant nonlinear nanophotonics. The lack of inversion symmetry—even in the bulk of the material—provides a combination of massive second-order susceptibility, extremely high and anisotropic refractive index in the near-infrared region ($n > 4.5$) and low absorption losses, making 3R-MoS_2 highly attractive for nonlinear nanophotonics. We demonstrate this by fabricating 3R-MoS_2 nanodisks of various radii, which support resonant anapole states, and observing substantial (>100-fold) enhancement of second-harmonic generation in a single resonant nanodisk compared with an unpatterned flake of the same thickness. The enhancement is maximized at the spectral overlap between the anapole state of the disk and the material resonance of the second-order susceptibility. Our approach unveils a powerful tool for enhancing the entire spectrum of optical second-order nonlinear processes in nanostructured van der Waals materials, thereby paving the way for nonlinear and quantum high-index transition metal dichalcogenide nanophotonics.

Nonlinear optics play a pivotal role in modern science and technology, particularly through second-order nonlinearities that enable crucial processes like second-harmonic generation (SHG), optical parametric oscillation and parametric down-conversion[1–3]. These nonlinear phenomena require a break of inversion symmetry in the bulk of the material. Consequently, promising material platforms for nonlinear optics applications typically encompass symmetry-broken dielectrics with low optical absorption. Specifically, the degree of second-order nonlinearity is quantified by the second-order nonlinear susceptibility $\chi^{(2)}$, which gives rise to nonlinear polarization $P_i^{(2)}$ in accordance with

$$P_i^{(2)} = \sum_{j,k} \varepsilon_0 \chi_{ijk}^{(2)} E_j E_k, \quad (1)$$

where E_j and E_k are electric-field components and ε_0 is the vacuum permittivity.

A full list of affiliations appears at the end of the paper. ✉e-mail: georgii.zograf@chalmers.se; timurs@chalmers.se

https://doi.org/10.1038/s41566-024-01444-9

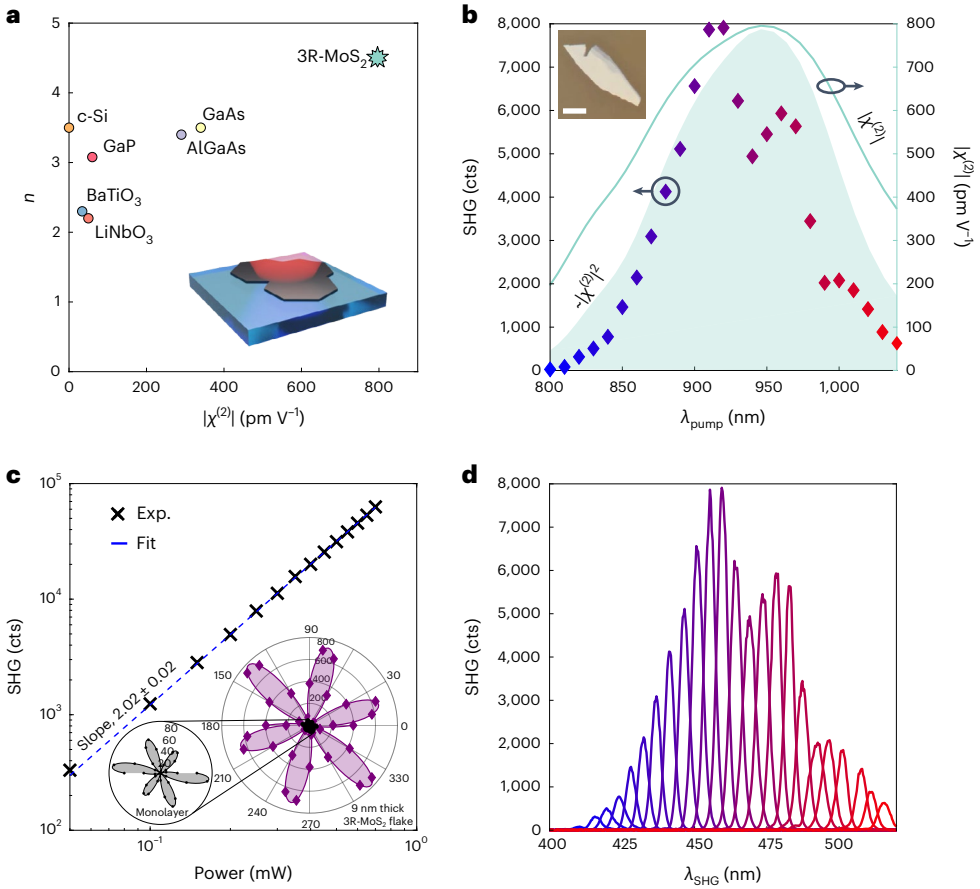

Fig. 1 | 3R-MoS_2 material nonlinear optical properties in the 800–1040 nm range. a, Comparison of linear and nonlinear optical properties for several selected materials: maximum $|\chi^{(2)}|$ component of each material versus refractive index n in the near-infrared spectral region. The inset shows the schematic of the optically non-resonant 3R-MoS_2 flake studied in **b**–**d**. Optical data for various materials are taken from $BaTiO_3$ (ref. 11), c-Si (refs. 1,4), GaP (ref. 23), GaAs (refs. 1,14), AlGaAs (ref. 17), $LiNbO_3$ (ref. 14) and 3R-MoS_2 (ref. 44) for refractive index and the DFT data for nonlinear susceptibility is shown in **b**. **b**, Coloured-diamond scatter plot shows the maximum SHG intensity of the optically non-resonant 9-nm-thick 3R-MoS_2 flake on a glass substrate as a function of the pump wavelength λ_{pump} at 0.2 mW average incident power for every pump wavelength. The inset shows the optical image of the flake. Scale bar, 30 µm. The cyan solid line shows $|\chi^{(2)}|$ calculated using DFT. Semi-transparent cyan shape corresponds to the normalized $|\chi^{(2)}|^2$ curve. **c**, Power-to-power log–log-scale plot of SHG intensity versus pump power. The inset shows the polar plots of polarization-resolved SHG obtained at 910 nm pump for a 9-nm-thick 3R-MoS_2 flake (purple) and MoS_2 monolayer (black). **d**, SHG spectra of the 3R-MoS_2 flake for different pump wavelengths λ_{pump} from 800 to 1040 nm with 0.2 mW power. λ_{SHG} corresponds to $\lambda_{pump}/2$. The colour code of the lines corresponds to that of the diamonds in **b**.

Figure 1a illustrates a comparative analysis of commonly used nonlinear materials alongside crystalline silicon (c-Si). The latter, although widely regarded as a prominent nanophotonics material due to its high refractive index of $n \approx 3.5$ in the lossless near-infrared region[4], lacks $\chi^{(2)}$ due to its centrosymmetry[1]. Lithium niobate ($LiNbO_3$) and barium titanate ($BaTiO_3$) are among the most extensively employed nonlinear materials renowned for their performance in second-order nonlinear processes and integrated photonics applications[5–13]. The advantage of these wide-band semiconductors is their exceptionally low material losses. In the near-infrared region, $LiNbO_3$ and $BaTiO_3$ support moderate $\chi^{(2)}$ (largest components) of the order of 50 pm V^{-1} (ref. 14) and 34 pm V^{-1} (ref. 11), respectively, varying depending on the different reports, in the region around 1060 nm wavelengths. A notable weakness of these two materials is the relatively low refractive index in the near-infrared region, which is slightly greater than 2, making the optical contrast between the material and substrate dramatically low. Such a low contrast, although allowing for them to perform well in low-loss waveguides and high-quality-factor (high-Q) resonators (such as whispering gallery modes, microrings and so on) for integrated photonics applications and discrete optical components[15,16], makes it difficult to create compact subwavelength resonant nanostructures supporting optical nonlinear effects.

Having a refractive index similar to that of c-Si, both GaAs and AlGaAs benefit from a significant value of $\chi^{(2)}$—of the order of 340 pm V^{-1} (ref. 14) and 290 pm V^{-1} (ref. 17), respectively (Fig. 1a). These materials have already demonstrated outstanding performance with record-high SHG[17–19] and spontaneous parametric down-conversion[20,21]. However, one of the major disadvantages of using GaAs/AlGaAs is the complexity and high cost of fabrication, which requires molecular-beam epitaxy techniques. Furthermore, the fabrication process can be potentially intricate due to the requirement of high-index substrates during the growth phase, followed by the transfer to low-index substrates[17,22]. Gallium phosphide (GaP) faces similar challenges, but it provides lower second-order nonlinearity (~70 pm V^{-1}) and lower refractive index[23] in the near-infrared regime than the GaAs family.

Transition metal dichalcogenides (TMDs) have recently emerged as a promising high-index nanophotonics platform in the near-infrared range, with a significant second-order nonlinear susceptibility in their atomically thin structures[24–29]. However, their bulk counterparts are unlikely to exhibit substantial $\chi^{(2)}$ due to the commonly adopted A_1B_2 stacking configuration. This is evident from a vanishing SHG from 2H-MoS_2 and multilayers of similar materials containing an even number of layers in the few-layer regime and in the bulk of the material[24,25]. Nevertheless, the utilization of nanophotonic

resonances in centrosymmetric multilayer TMD nanostructures has shown a remarkable enhancement in SHG[30–32]. Furthermore, the SHG intensity of TMD monolayers placed on external metasurfaces has been substantially boosted[33,34]. However, this approach does not allow the implementation of an all-TMD nonlinear nanophotonics concept[35–40]. As a result, there is a growing demand for alternative material platforms that can combine high refractive indices with exceptional nonlinearities.

Unlike the 2H counterpart, the 3R phase of MoS_2 does not restore inversion symmetry, allowing it to possess second-order nonlinearity even in the bulk crystal. Recently, it was shown that 3R-MoS_2 has one of the most substantial $\chi^{(2)}$ values, which is useful for SHG[41,42] and piezoelectricity[43] applications. Furthermore, the low optical absorption in the near-infrared range[44] makes 3R-MoS_2 advantageous for nonlinear optics applications compared with lossy Weyl semimetals with giant $\chi^{(2)}$ values[45]. Additionally, 3R-MoS_2 supports ultrahigh refractive index ($n > 4.5$) (ref. 44) and has prospects for epitaxial as well as chemical vapour deposition wafer-scale fabrication[46–48]. Therefore, 3R-MoS_2 is an excellent candidate for nonlinear all-dielectric nanophotonics (Fig. 1a). We note that the refractive index of 3R-MoS_2 in this study was assumed to be identical to that of its 2H counterpart[44], given the similarity in excitonic properties, which predominantly define the linear optical response within the relevant spectral range. As shown below, experiments show good agreement with theory, further justifying this assumption.

Our density functional theory (DFT) calculations predict that $\chi^{(2)}$ of 3R-MoS_2 is particularly high (Supplementary Figs. 1 and 2). Specifically, the solid line in Fig. 1b corresponds to several selected $\chi^{(2)}_{ijk}$ tensor components (see the right y axis). The cyan-coloured line depicts the most dominant ones—$\chi^{(2)}_{xyx}$, $\chi^{(2)}_{yyy}$ and $\chi^{(2)}_{yxx}$—which have pronounced resonant behaviour peaking at λ_{pump} of ~950 nm and reaching values as high as ~800 pm V^{-1}. Therefore, 3R-MoS_2 exhibits superior performance compared with conventional nonlinear materials (Fig. 1a) in terms of both second-order nonlinearity and refractive index. The measured SHG as a function of the pump wavelength for a 9-nm-thick, optically non-resonant flake qualitatively agrees with the DFT calculations and peaks at around 910–920 nm (an optically non-resonant flake is defined as one that is too thin to sustain Fabry–Pérot resonances; consequently, its SHG response should not include a contribution associated with optical-field enhancement but rather incorporate only material $\chi^{(2)}$ dispersion). Moreover, an even better agreement is met when the experimental SHG intensity is plotted against $|\chi^{(2)}_{xyx}|^2$, since $I_{SHG} \propto |\chi^{(2)}|^2$. We attribute the observed bell-shaped SHG spectrum to a material resonance of nonlinearity in 3R-MoS_2. This resonance is of excitonic origin, similar to previously observed SHG in monolayer MoS_2 (ref. 24) and WSe_2 (ref. 26). Specifically, the bell-shaped nature of the $\chi^{(2)}$ spectrum is caused by the overlap of the second-harmonic signal at 475 nm with the C exciton, in agreement with previous findings[42] and our DFT calculations (Supplementary Fig. 1). This can be inferred from the fact that both ω and 2ω transitions are relevant for the quadratic polarizability: (1) no intense transitions (at ω) are present in the 800–1000 nm range (below the A exciton); (2) the 400–500 nm range overlaps with transitions comprising the C exciton (at 2ω). Supplementary Section 1 and another work[49] provide further details.

To verify the second-order nature of the observed nonlinear process, we plot the power-to-power dependence of SHG at the near-optimal 940 nm pump. Figure 1c shows the incident pump power versus SHG intensity in a log–log scale. The slope of the fitting function is 2.02 ± 0.02 with a 95% confidence, manifesting the second-order nonlinear process. The damage threshold for this flake at the optimal wavelength of 910 nm occurs at laser powers between 50 and 72 mW (Supplementary Fig. 3 and Supplementary Information), which is in agreement with previous reports[41,42]. Note that the laser used in this experiment has a repetition rate of 80 MHz and a pulse duration of ~100 fs, implying that an averaged power of 50 mW corresponds to a peak power of ~6.25×10^3 W. The latter is nearly 500 times higher than the damage threshold of AlGaAs nanodisks on SiO_2/indium tin oxide (ref. 17), making 3R-MoS_2 attractive for high-power nonlinear optics applications. Moreover, such laser powers at 910 nm pump wavelength in our experiments were tightly focused to the diffraction-limited spot (objective, ×40; numerical aperture (NA), 0.95) corresponding to intensities of $I_{pump} \approx 3.7 \times 10^6$ W cm^{-2} and peak power densities of $I_{peak} \approx 4.6 \times 10^{11}$ W cm^{-2}.

Furthermore, we performed polarization-resolved SHG measurements on the same flake (optical image is shown in Fig. 1b, inset). The result displays a six-fold symmetry profile (Fig. 1c, purple polar plot). For comparison, we also provide the SHG data of a MoS_2 monolayer (black). The monolayer signal is more than ten times weaker than that of the 9-nm-thick 3R-MoS_2 flake measured under the same conditions (Supplementary Fig. 4 shows a detailed comparison). Additionally, we measured the SHG spectra as a function of excitation wavelength in the 800–1040 nm range at a fixed pump power to demonstrate the precise correspondence between the pump and emission wavelength, namely, $\lambda_{SHG} = \lambda_{pump}/2$ (Fig. 1d). The colour codes used in Fig. 1d are the same as in Fig. 1b. Remarkably, the SHG spectra are intense and lack any residual or background signal, allowing us to use an alternative SHG detection scheme—an avalanche photodiode—which is advantageous for extended SHG mapping experiments discussed below.

Optically resonant nanostructures

We successfully optimized the optical pump conditions to achieve the maximum SHG intensity in optically non-resonant 3R-MoS_2 flakes, solely relying on the resonant properties of the material. In addition, the DFT calculations were performed using the bulk model of 3R-MoS_2, which excluded any consideration of optical resonances. Our current objective is to go beyond this and engineer the resonant optical response, in combination with the material properties, to further enhance the efficiency of SHG. The core concept of this work is to ensure that the engineered resonant optical response of the nanostructures aligns spectrally with the material resonances of 3R-MoS_2, creating an effective overlap between them. Indeed, the SHG can be dramatically enhanced by using high-Q optical resonators. If the resonance is tuned to the pump wavelength, the SHG output power scales as $P^{2\omega} \propto (Q_1 P^{\omega})^2$ (refs. 17,19,32), where P^{ω} is the pump power, ω is the pump photon frequency and Q_1 is the quality factor of the resonance at the pump wavelength. Here we do not account for the optical mode at the SHG wavelength due to the high optical losses of 3R-MoS_2 in that range.

We proceed with the design and fabrication of 3R-MoS_2 subwavelength optical resonators. Due to challenges in fabricating spherical nanoresonators capable of hosting optical Mie modes[50,51], TMD nanodisks are preferred for their highest possible symmetry[35,52]. Specifically, TMD nanodisks are insensitive to incident linear polarization, at normal light excitation due to axial symmetry, and can support optical modes across the visible and near-infrared ranges. Therefore, in this work, we focus on fabricating and studying optically resonant subwavelength nanodisks. These nanodisks can support anapole states in the 880–960 nm region, which enables efficient spectral overlap with the material-specific $\chi^{(2)}$ resonance. The anapole states can substantially enhance the SHG signal by capturing optical excitations within the disk instead of radiating them out to the far field[18,30,53,54].

We start with a numerical design of an appropriate nanodisk geometry. Our analysis involves studying resonantly enhanced electromagnetic energy stored within the volume of the nanodisk, namely, $u_{NP} \propto |E|^2$, where $|E|^2 = EE^*$; E^* stands for the complex conjugation of the electric field. Figure 2a shows the colour map of normalized $|E|^2$ in the volume of an individual 3R-MoS_2 nanodisk of 65 nm height and a

https://doi.org/10.1038/s41566-024-01444-9

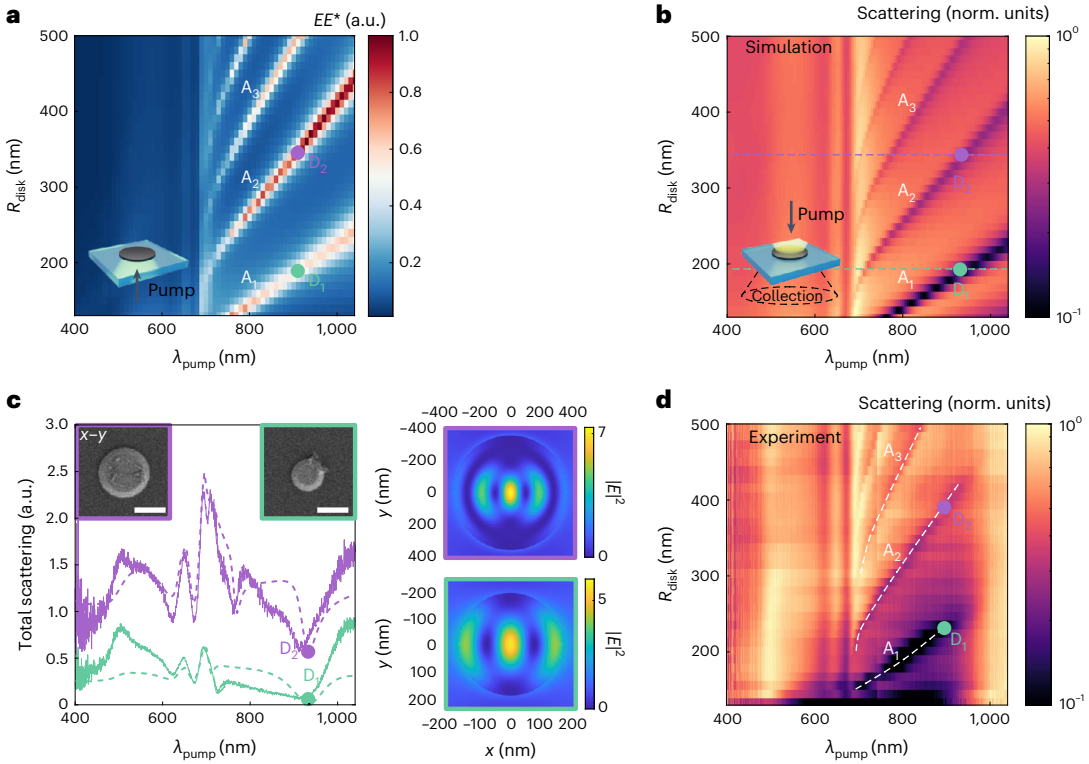

Fig. 2 | Linear optical properties of 3R-MoS_2 nanodisks. a, Numerical calculation of $|E|^2$, characterizing the stored electromagnetic energy inside the 3R-MoS_2 nanodisk, in normalized units. A_1, A_2 and A_3 are anapole-like states. The inset shows the schematic of the calculation geometry. D_1 and D_2 label the nanodisks with resonantly enhanced stored electromagnetic energy. **b**, Numerical calculation of the elastic light scattering spectra by individual 3R-MoS_2 nanodisks as a function of the nanodisk's radius in the DF geometry using conditions similar to experimental ones. **c**, Lilac (R_{disk} = 350 nm) and mint (190 nm) lines correspond to D_2 and D_1 numerical (dashed) and experimental (solid) DF scatterings. The inset shows the SEM images of the two selected nanodisks. Scale bar, 500 nm. The side panels show the corresponding near-field distributions calculated at 920 nm pump. **d**, Colour map shows the experimental DF scattering spectra for 3R-MoS_2 nanodisks in the logarithmic scale. Each scattering spectrum obtained for a particular radius R_{disk} is normalized to its maximum value. The white dashed lines indicate the dispersion of anapole states with the nanodisk's radius.

range of radii R_{disk} from 130 to 500 nm under normal plane-wave excitation from the bottom (glass substrate) side. Such excitation geometry is chosen because it resembles the experimental SHG setup (discussed below), which allows for improved scattering signal collection due to a higher k vector in the glass substrate. The choice of a 3R-MoS_2 nanodisk height of h = 65 nm is based on our numerical analysis, which indicates that the optimal SHG response occurs within the range of heights $h \approx 60$–90 nm for a free-standing nanodisk (Supplementary Fig. 5). Furthermore, our numerical analysis allows for using directional excitation and specific apertures for collecting the scattered light (Methods). Evidently, the nanodisks host three resonant features (denoted as A_1, A_2 and A_3) that show enhanced $|E|^2$ in the spectral region of the highest nonlinear response. The region below 700 nm demonstrates no resonant features due to high optical losses. We mark the optimal disks with points D_1 and D_2, corresponding to the highest stored electromagnetic energy at the wavelength of the material $\chi^{(2)}$ resonance (~920 nm). These disks are promising for subsequent SHG experiments and their theoretically predicted parameters are R_{disk} = 190 and 350 nm, respectively.

To assign the resonant features A_1, A_2 and A_3 to optical anapoles, we first calculate the scattering response of the nanodisks. Figure 2b shows a colour map of the calculated scattering cross-section for various 3R-MoS_2 nanodisk sizes. Note that in this case, the light is incident on the sample from the top, to mimic the experimental dark-field (DF) scattering setup, as discussed below. The scattering cross-section at each specific nanodisk radius is normalized to unity to enhance the visual representation of the data. Indeed, the A_1, A_2 and A_3 features demonstrate anapole-like behaviour, which is manifested in a substantial drop in their scattering signals. The scattering spectra of D_1 and D_2 nanodisks (mint- and lilac-coloured dashed lines) alongside their calculated electromagnetic near-field maps are shown in Fig. 2c. The near-field maps were evaluated at the minima of the scattering spectra (labelled D_1 and D_2) and show that the electric fields are mostly confined within the nanodisk volume and exhibit typical anapole profiles. We, thus, conclude that within the studied parameter range, the appearance of optical anapoles in 3R-MoS_2 nanodisks is feasible[35].

Based on the theoretical predictions, we fabricated 65-nm-high 3R-MoS_2 nanodisks with radii in the range of 130–500 nm. Such a design results in a number of resonant features in the 880–960 nm spectral range, making it highly promising for the simultaneous enhancement of SHG through the combined effect of optical and material resonances. Additional details about the nanodisk fabrication and their optical and morphological analysis are provided in the 'Morphological characterization' section and Supplementary Fig. 6.

We performed the morphological characterization of the fabricated nanodisks (Supplementary Fig. 7) by scanning electron microscopy (SEM) and atomic force microscopy (AFM) (Supplementary Fig. 8). Figure 2c depicts the experimental DF scattering of two individual nanodisks with experimental radii of ~225 nm (mint solid) and ~380 nm (lilac solid). These spectra are plotted against the theoretical 190- and 350-nm-radii disks (correspondingly coloured dashed line). The agreement between theory and experiment is good, with an important remark that there is a slight offset between the sizes used in the calculation model and the actual experimental sizes. This difference may arise due to the disk's geometry deviating from a perfect cylinder and having a slight frustum shape (bottom and top radii are slightly different). The insets in Fig. 2c depict the corresponding SEM images of experimentally fabricated nanodisks, demonstrating this point. Taking this into account, the experimental DF scattering response is slightly shifted

https://doi.org/10.1038/s41566-024-01444-9

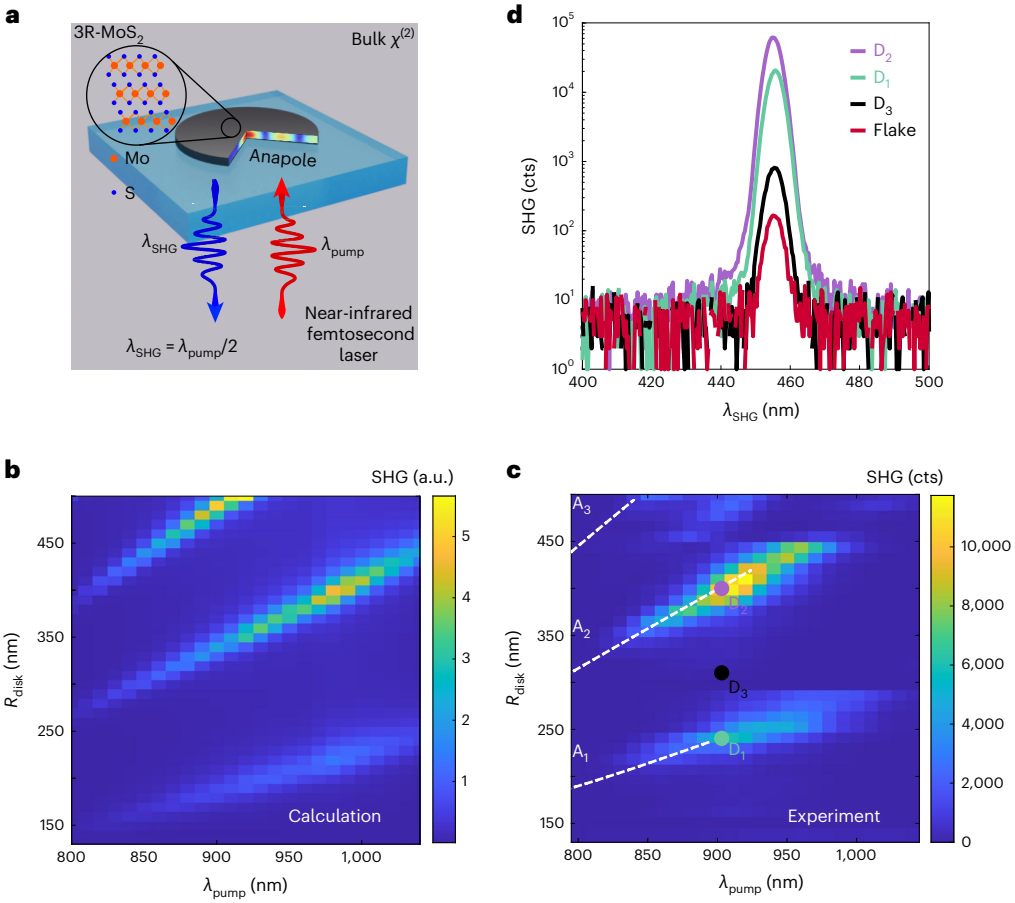

Fig. 3 | SHG in 3R-MoS_2 nanodisks. a, Schematic of the experiment: an individual 3R-MoS_2 nanodisk is excited with a near-infrared femtosecond laser and efficiently converts the pump light into SHG due to a combination of the anapole state hosted by the nanodisk and a substantial $\chi^{(2)}$ nonlinearity. A quarter of the nanodisk has been removed to visualize the near-field distribution at the anapole state. **b**, Numerical calculation of the SHG intensity of 3R-MoS_2 nanodisks with varying disk radii on a glass substrate at different pump wavelengths. The SHG intensity is obtained as the total radiation generated at $\lambda_{SHG} = \lambda_{pump}/2$. **c**, Experimentally measured SHG colour map of individual 3R-MoS_2 nanodisks on a glass substrate at different pump wavelengths. The intensity of the SHG signal is obtained at $\lambda_{pump}/2$ for every nanodisk. **d**, SHG spectra measured at 910 nm pump for an unpatterned 3R-MoS_2 flake (red line), resonant nanodisks (D_1 (mint) and D_2 (lilac)) and an arbitrary off-resonant nanodisk D_3 (black). Note that the *y* axis is shown in a logarithmic scale.

compared with the numerical design (Fig. 2d) (Supplementary Fig. 9 shows the explicit one-dimensional scattering plots in the linear scale and optical DF images). In Fig. 2d, we highlight the anapole-like dips A_{1-3} observed in experimental DF scattering spectra and their dispersion with the size of the nanodisks.

Resonantly enhanced SHG in individual 3R-MoS_2 nanodisks

We now turn our attention to the harmonic generation of individual 3R-MoS_2 nanodisks. Specifically, we study their nonlinear optical properties in a configuration schematically shown in Fig. 3a. The SHG intensity calculation for nanodisks adopting this excitation–collection geometry is shown in Fig. 3b (Methods provides more details of this calculation). A COMSOL Multiphysics (version 6.0) numerical model was used in two steps: (1) the near-infrared wavelength excitation λ_{pump} of the nanodisk followed by an extraction of the near-field data; (2) evaluation of the nonlinear polarization of the disk at $\lambda_{pump}/2$ using near-fields from (1) weighted by the $\chi^{(2)}$ tensor, and finally, SHG at $\lambda_{pump}/2$. Remarkably, the areas of the highest SHG intensity in the spectra appear at the overlap between the $\chi^{(2)}$ tensor resonance (Fig. 1b) and in good agreement with the A_1, A_2 and A_3 curves predicted in the linear response (Fig. 2a).

We further proceed to the SHG measurements. Figure 3c shows the SHG maps obtained for nanodisk radii in the 130–500 nm range and pump wavelengths of 800–1040 nm (fixed power, ~300 μW) (Supplementary Fig. 10 shows the log-scale data). The data were recorded by scanning the sample with respect to the focused laser spot over the entire nanodisk array (disk-to-disk separation, 5 μm) at a given pump wavelength using a piezostage (Methods). The nonlinear signal was collected using an avalanche photodiode. Detailed SHG intensity maps of the nanodisk arrays are shown in Supplementary Figs. 11–13. As evaluated by the stored electromagnetic energy and linear DF scattering analysis (Fig. 2), the nanodisks with experimental radii of ~225 nm (D_1) and ~380 nm (D_2) support anapole-like behaviour at the wavelength at which we observe the maximum experimental $\chi^{(2)}$ (Fig. 1). These disks, therefore, are expected to display the highest SHG intensity peaking at ~910–920 nm λ_{pump}, which matches the condition of the highest experimental value of $\chi^{(2)}$ for the material. Remarkably, the experimentally measured anapole-enhanced SHG for a 380 nm nanodisk (D_2) at 910 nm pump provides close to two orders (~80-fold) of magnitude increase in the SHG signal compared with the arbitrary off-resonant nanodisk at this wavelength (labelled as D_3 with $R_{disk} \approx 310$ nm). Such a remarkable enhancement in SHG intensity can be attributed to the resonant anapole states of D_1 and D_2, possessing *Q*-factors of ~11 and ~20, respectively. The *Q*-factors were estimated from the scattering spectra shown in Fig. 2c as their resonant frequencies normalized by the full-width at half-maximum values. The optical part of the total SHG enhancement is approximately given as Q^2, which implies a *Q*-factor

of ~10, in line with our findings. Moreover, the difference between the simultaneously optically and materially resonant D_2 nanodisk pumped at λ_{pump} = 910 nm and an off-resonant (both optically and materially) one can be significantly higher and approaches ~four orders of magnitude (limited by the detection resolution, ~5000-fold) (Supplementary Fig. 10). An SHG enhancement exceeding two orders of magnitude is reached between the resonant anapole nanodisk and the parent flake from which the disk was fabricated. However, in the case of the unpatterned flake, the volume of the emitting SHG material is probably much larger due to the diffraction limit of the pump beam. Remarkably, the highest SHG intensity areas spectrally match with the DF scattering anapole dips, confirming the hypothesis that the SHG signal is dramatically enhanced by the optical anapole states. Furthermore, the agreement with the calculations of the SHG response of the nanodisks on a glass substrate (Fig. 3b) is also remarkable. A slight mismatch between the calculations and experiments is mainly due to two reasons: (1) the DFT-calculated $\chi^{(2)}$ tensor, used for numerical calculations, peaks at around 950–960 nm pump wavelength, whereas the experimental one is around 910–920 nm (Fig. 1b); (2) the SEM images demonstrate that the fabricated nanodisks slightly deviate from the perfect cylindrical shape, which affects their optical response.

To further improve our understanding of the SHG enhancement mechanism, we have performed an explicit head-to-head comparison of the SHG signals from the two most resonant disks D_1, D_2, the non-resonant disk D_3 (at the same λ_{pump} = 910 nm wavelength, but without anapole enhancement) and the unpatterned parent flake. Additionally, we collected the SHG signal of these disks under off-material resonance conditions for 820 and 1020 nm pumping. These measurements show SHG signals slightly above the background noise level (Supplementary Fig. 14). Such a comparison allows us to roughly estimate the relative contributions of material and optical enhancements to the SHG signal. Specifically, our analysis reveals that the optical anapole enhancement is responsible for about 80-fold enhancement (from the comparison between D_1, D_2 and D_3). The material resonance provides an additional 100-fold increase at the 910 nm pump wavelength compared with 820–1020 nm pumps (Fig. 1b). Jointly, the optical and material resonances allow SHG signal tuning in an enhancement range that approaches four orders of magnitude within the near-infrared spectral range (~5000-fold). This is illustrated in Fig. 3d, which depicts the SHG spectra (log scale) obtained using a 910 nm pump wavelength at a low pump power of 0.3 mW and just 1 s collection time. The two most resonant disks—D_2 (lilac line) and D_1 (mint line)—possess an SHG signal that is more than two orders of magnitude stronger than the unpatterned 3R-MoS_2 parent flake (red), whereas the off-resonant nanodisk D_3 is only slightly stronger than the unpatterned flake. One of the most off-resonant disks in which an SHG signal can be detected with the spectrometer under the same experimental conditions is the D_1 disk pumped at 820 nm. As a consequence of being driven outside the anapole state and at the edge of the $\chi^{(2)}$ resonance, its SHG spectrum at 410 nm peaks slightly above the noise floor and is approximately one and two orders of magnitude weaker than, respectively, both the unpatterned flake and the optically off-resonant disk D_3 when driven at the material resonance (Fig. 3d and Supplementary Fig. 14).

In conclusion, we demonstrated that the SHG emission can be dramatically enhanced in the bulk $\chi^{(2)}$ 3R-MoS_2 material by combining the material and nanophotonic resonances. The material response was optimized by exciting the resonance of $\chi^{(2)}$ at ~910 nm pump wavelength, whereas nanophotonic resonances were engineered through appropriate nanodisk dimensions supporting the anapole state in the wavelength range overlapping with the material resonance. Such an approach provides more than three orders of magnitude enhancement of the SHG signal for the most resonant nanodisks versus the most off-resonant case (~5000-fold) and more than two orders of magnitude enhancement compared with the unpatterned flake of the same thickness (~400-fold). We anticipate that by manipulating the thickness of the 3R-MoS_2 flake, one can potentially achieve even higher enhancement of SHG by engineering nanophotonic resonances. Moreover, we envision that nanostructured 3R-MoS_2 holds great potential as a versatile platform for a wide range of all-TMD nonlinear nanophotonics applications beyond SHG. This includes various $\chi^{(2)}$ nonlinear processes such as the generation of entangled photon pairs[21], optical parametric amplification and electro-optical effects, where the resonator and nonlinear medium are integrated within the same nanostructured object, resonant metasurface or nanophotonic circuit.

Online content

Any methods, additional references, Nature Portfolio reporting summaries, source data, extended data, supplementary information, acknowledgements, peer review information; details of author contributions and competing interests; and statements of data and code availability are available at https://doi.org/10.1038/s41566-024-01444-9.

References

1. Boyd, R. W. *Nonlinear Optics* (Academic Press, 2020).
2. Dousse, A. et al. Ultrabright source of entangled photon pairs. *Nature* **466**, 217–220 (2010).
3. Lu, X. et al. Chip-integrated visible–telecom entangled photon pair source for quantum communication. *Nat. Phys.* **15**, 373–381 (2019).
4. Aspnes, D. E. & Studna, A. Dielectric functions and optical parameters of Si, Ge, GaP, GaAs, GaSb, InP, InAs, and InSb from 1.5 to 6.0 eV. *Phys. Rev. B* **27**, 985 (1983).
5. Carletti, L. et al. Second harmonic generation in monolithic lithium niobate metasurfaces. *Opt. Express* **27**, 33391–33398 (2019).
6. Solntsev, A. S., Kumar, P., Pertsch, T., Sukhorukov, A. A. & Setzpfandt, F. $LiNbO_3$ waveguides for integrated SPDC spectroscopy. *APL Photonics* **3**, 021301 (2018).
7. Fedotova, A. et al. Second-harmonic generation in resonant nonlinear metasurfaces based on lithium niobate. *Nano Lett.* **20**, 8608–8614 (2020).
8. Okoth, C., Cavanna, A., Santiago-Cruz, T. & Chekhova, M. Microscale generation of entangled photons without momentum conservation. *Phys. Rev. Lett.* **123**, 263602 (2019).
9. Santiago-Cruz, T. et al. Photon pairs from resonant metasurfaces. *Nano Lett.* **21**, 4423–4429 (2021).
10. Pohl, D. et al. An integrated broadband spectrometer on thin-film lithium niobate. *Nat. Photon.* **14**, 24–29 (2020).
11. Karvounis, A., Timpu, F., Vogler-Neuling, V. V., Savo, R. & Grange, R. Barium titanate nanostructures and thin films for photonics. *Adv. Opt. Mater.* **8**, 2001249 (2020).
12. Timpu, F., Sergeyev, A., Hendricks, N. R. & Grange, R. Second-harmonic enhancement with Mie resonances in perovskite nanoparticles. *ACS Photonics* **4**, 76–84 (2017).
13. Savo, R. et al. Broadband Mie driven random quasi-phase-matching. *Nat. Photon.* **14**, 740–747 (2020).
14. Shoji, I., Kondo, T., Kitamoto, A., Shirane, M. & Ito, R. Absolute scale of second-order nonlinear-optical coefficients. *J. Opt. Soc. Am. B* **14**, 2268–2294 (1997).
15. Fedotova, A. et al. Lithium niobate meta-optics. *ACS Photonics* **9**, 3745–3763 (2022).
16. Zhang, M. et al. Broadband electro-optic frequency comb generation in a lithium niobate microring resonator. *Nature* **568**, 373–377 (2019).
17. Koshelev, K. et al. Subwavelength dielectric resonators for nonlinear nanophotonics. *Science* **367**, 288–292 (2020).
18. Timofeeva, M. et al. Anapoles in free-standing III–V nanodisks enhancing second-harmonic generation. *Nano Lett.* **18**, 3695–3702 (2018).

19. Frizyuk, K. Second-harmonic generation in dielectric nanoparticles with different symmetries. *J. Opt. Soc. Am. B* **36**, F32–F37 (2019).
20. Marino, G. et al. Spontaneous photon-pair generation from a dielectric nanoantenna. *Optica* **6**, 1416–1422 (2019).
21. Santiago-Cruz, T. et al. Resonant metasurfaces for generating complex quantum states. *Science* **377**, 991–995 (2022).
22. Camacho-Morales, R. et al. Nonlinear generation of vector beams from AlGaAs nanoantennas. *Nano Lett.* **16**, 7191–7197 (2016).
23. Tilmann, B. et al. Comparison of harmonic generation from crystalline and amorphous gallium phosphide nanofilms. *Adv. Opt. Mater.* **11**, 2300269 (2023).
24. Kumar, N. et al. Second harmonic microscopy of monolayer MoS_2. *Phys. Rev. B* **87**, 161403 (2013).
25. Li, Y. et al. Probing symmetry properties of few-layer MoS_2 and h-BN by optical second-harmonic generation. *Nano Lett.* **13**, 3329–3333 (2013).
26. Wang, G. et al. Giant enhancement of the optical second-harmonic emission of WSe_2 monolayers by laser excitation at exciton resonances. *Phys. Rev. Lett.* **114**, 097403 (2015).
27. Trovatello, C. et al. Optical parametric amplification by monolayer transition metal dichalcogenides. *Nat. Photon.* **15**, 6–10 (2021).
28. Khan, A. R. et al. Optical harmonic generation in 2D materials. *Adv. Funct. Mater.* **32**, 2105259 (2022).
29. Kumar, P. et al. Light–matter coupling in large-area van der Waals superlattices. *Nat. Nanotechnol.* **17**, 182–189 (2022).
30. Busschaert, S. et al. Transition metal dichalcogenide resonators for second harmonic signal enhancement. *ACS Photonics* **7**, 2482–2488 (2020).
31. Nauman, M. et al. Tunable unidirectional nonlinear emission from transition-metal-dichalcogenide metasurfaces. *Nat. Commun.* **12**, 5597 (2021).
32. Popkova, A. A. et al. Nonlinear exciton-Mie coupling in transition metal dichalcogenide nanoresonators. *Laser Photonics Rev.* **16**, 2100604 (2022).
33. Hu, G. et al. Coherent steering of nonlinear chiral valley photons with a synthetic Au–WS_2 metasurface. *Nat. Photon.* **13**, 467–472 (2019).
34. Bernhardt, N. et al. Quasi-BIC resonant enhancement of second-harmonic generation in WS_2 monolayers. *Nano Lett.* **20**, 5309–5314 (2020).
35. Verre, R. et al. Transition metal dichalcogenide nanodisks as high-index dielectric Mie nanoresonators. *Nat. Nanotechnol.* **14**, 679–683 (2019).
36. Munkhbat, B. et al. Transition metal dichalcogenide metamaterials with atomic precision. *Nat. Commun.* **11**, 4604 (2020).
37. Ling, H., Li, R. & Davoyan, A. R. All van der Waals integrated nanophotonics with bulk transition metal dichalcogenides. *ACS Photonics* **8**, 721–730 (2021).
38. Sung, J. et al. Room-temperature continuous-wave indirect-bandgap transition lasing in an ultra-thin WS_2 disk. *Nat. Photon.* **16**, 792–797 (2022).
39. Munkhbat, B., Küçüköz, B., Baranov, D. G., Antosiewicz, T. J. & Shegai, T. O. Nanostructured transition metal dichalcogenide multilayers for advanced nanophotonics. *Laser Photonics Rev.* **17**, 2200057 (2023).
40. Zotev, P. G. et al. Van der Waals materials for applications in nanophotonics. *Laser Photonincs Rev.* **17**, 2200957 (2023).
41. Shi, J. et al. 3R MoS_2 with broken inversion symmetry: a promising ultrathin nonlinear optical device. *Adv. Mater.* **29**, 1701486 (2017).
42. Xu, X. et al. Towards compact phase-matched and waveguided nonlinear optics in atomically layered semiconductors. *Nat. Photon.* **16**, 698–706 (2022).
43. Dong, Y. et al. Giant bulk piezophotovoltaic effect in 3R-MoS_2. *Nat. Nanotechnol.* **18**, 36–41 (2023).
44. Munkhbat, B., Wróbel, P., Antosiewicz, T. J. & Shegai, T. O. Optical constants of several multilayer transition metal dichalcogenides measured by spectroscopic ellipsometry in the 300–1700 nm range: high index, anisotropy, and hyperbolicity. *ACS Photonics* **9**, 2398–2407 (2022).
45. Wu, L. et al. Giant anisotropic nonlinear optical response in transition metal monopnictide Weyl semimetals. *Nat. Phys.* **13**, 350–355 (2017).
46. Li, T. et al. Epitaxial growth of wafer-scale molybdenum disulfide semiconductor single crystals on sapphire. *Nat. Nanotechnol.* **16**, 1201–1207 (2021).
47. Liu, L. et al. Uniform nucleation and epitaxy of bilayer molybdenum disulfide on sapphire. *Nature* **605**, 69–75 (2022).
48. Shinde, S. M. et al. Stacking-controllable interlayer coupling and symmetric configuration of multilayered MoS_2. *NPG Asia Mater.* **10**, e468 (2018).
49. Sharma, S. & Ambrosch-Draxl, C. Second-harmonic optical response from first principles. *Phys. Scr.* **T109**, 128–134 (2004).
50. Tselikov, G. I. et al. Transition metal dichalcogenide nanospheres for high-refractive-index nanophotonics and biomedical theranostics. *Proc. Natl Acad. Sci. USA* **119**, e2208830119 (2022).
51. Chernikov, A. S. et al. Tunable optical properties of transition metal dichalcogenide nanoparticles synthesized by femtosecond laser ablation and fragmentation. *J. Mater. Chem. C* **11**, 3493–3503 (2023).
52. Green, T. D. et al. Optical material anisotropy in high-index transition metal dichalcogenide Mie nanoresonators. *Optica* **7**, 680–686 (2020).
53. Baranov, D. G., Verre, R., Karpinski, P. & Käll, M. Anapole-enhanced intrinsic Raman scattering from silicon nanodisks. *ACS Photonics* **5**, 2730–2736 (2018).
54. Ushkov, A. A. et al. Anapole states and scattering deflection effects in anisotropic van der Waals nanoparticles. *Phys. Rev. B* **106**, 195302 (2022).

[1]Department of Physics, Chalmers University of Technology, Göteborg, Sweden. [2]Faculty of Physics, University of Warsaw, Warsaw, Poland.
✉e-mail: georgii.zograf@chalmers.se; timurs@chalmers.se

Methods

Fabrication

The nanofabrication workflow for 3R-MoS_2 submicrometre disks is shown in Supplementary Fig. 6. The nanofabrication steps were performed in Myfab Nanofabrication Laboratory, MC2 Chalmers. High-quality 3R-MoS_2 crystal was purchased from HQ Graphene and mechanically exfoliated into multilayer flakes using Scotch tape. Polydimethylsiloxane stamps (Gel-Pak) were used to transfer the flakes onto one inch by one inch glass substrates (0.17 mm thickness). ARP 6200.13 resist (Allresist) was used to create an ~550-nm-thick mask for 3R-MoS_2 dry etching. A 25 nm Cr layer was electro-evaporated by a Kurt J. Lesker Nano 36 evaporator on top of the resist to eliminate the substrate-charging effects during electron-beam lithography. A Raith EBPG 5200 system operating at 100 kV accelerating voltage was used for the direct-writing electron-beam lithography. ARP was nanopatterned using a current of 10 nA and a dose within the 259–447 μC cm^{-2} range with the proximity effect correction. After the electron-beam exposure, the Cr layer was removed using a Ni–Cr etching solution (10–20% ammonium cerium(IV) nitrate, 5–40% nitric acid; Sunchem AB), and *n*-amyl acetate (SuperIco, Sigma-Aldrich) was used as a developer. CHF_3 plasma in an Oxford Plasmalab 100 system was used to dry etch 3R-MoS_2 flakes through the ARP mask. The leftover resist was removed using *N*-methyl-2-pyrrolidone (Remover 1165, DuPont Specialty EM) and acetone (BASF). Finally, the samples were washed with deionized water and gently blow-dried. The nanofabricated devices were stored in a clean-room environment till further experiments.

Morphological characterization

SEM. SEM of the nanodisks was performed at Chalmers Materials Analysis Laboratory using an Ultra 55 microscope (Carl Zeiss). An accelerating voltage of 1 kV was used to visualize the semiconducting nanodisks on a glass substrate without applying any conductive coating. A conductive copper tape was attached to the face side of the glass substrate close to the nanodisks to decrease the charging effects. Images were registered using a secondary electron detector. For the tilted-view imaging, the sample was mounted on a 45° pre-tilted holder, and a 1.6–2.0 kV accelerating voltage was used to operate at a safe working distance, although the charging of the sample surface became more noticeable.

AFM. AFM was carried out at Myfab Nanofabrication Laboratory, MC2 Chalmers, using a Dimension 3100 microscope (Veeco). The scans were performed in the tapping mode using 0.2–1.0 Hz scan rates.

Optical measurements

DF elastic light scattering. Linear resonant optical properties of the nanodisks were studied by means of DF elastic scattering of light using an inverted microscope (Nikon Eclipse TE2000E). The sample on a glass substrate was excited with a plane-wave broadband light source through a Nikon DF condenser (NA, 0.80–0.95) and collected from the bottom substrate with an oil-immersion objective (variable NA, 0.5–1.3; ×100, Nikon S Fluor). The collected signal was then analysed by an ANDOR Shamrock 500i spectrometer with a 150 lines mm^{-1} grating (Blaze 800) equipped with a Newton 920 charge-coupled device camera.

SHG. Tunable Spectra Physics MaiTai HP femtosecond Ti:sapphire 100 fs 80 MHz laser (tuning range, 690–1040 nm) was used to excite the sample at normal incidence through a Nikon Plan Apo (NA, 0.95, ×40) objective with a correction ring from the glass-substrate side of the sample. The emitted SHG signal was collected through the same objective and then analysed by an ANDOR Shamrock 500i spectrometer equipped with a Newton 920 charge-coupled device camera, or in the case of extended area scanning, by an avalanche photodiode (IDQ id100 single-photon detection module) with a PicoHarp 300 TC-SPC module that allowed us to process the intensity of the SHG emission. The precise positioning was controlled by an *xyz* piezostage (Mad City Labs, Nano-LP200). The incident laser power was controlled by a polarizer–analyser pair. The linear polarization of the incident femtosecond laser beam was controlled by a broadband half-wavelength plate.

Numerical calculations

DF scattering. The electromagnetic energy of a single 3R-MoS_2 nanodisk was calculated using commercial COMSOL Multiphysics software (version 6.0). Electromagnetic-wave physics with the frequency domain was used to analyse the scattering of a linearly polarized wave along the *x*-axis plane wave. The computational model consisted of the outer sphere of 2λ radius with a plane-wave section perpendicular to the *z* axis that represents the air–glass interface. The outer surface of the sphere served as a scattering boundary condition. Background field with *k* vector along the *z* axis was assigned with the Fresnel equation—having the incident light coming from the air, reflected from the glass and transmitted into the glass substrate. The electromagnetic energy was integrated over the nanodisk's volume.

The scattering cross-sections and near-field distributions were obtained from simulations carried out using Lumerical FDTD Solutions software (version 2021.2). Linearly polarized normal-incidence plane wave was used to illuminate the 3R-MoS_2 disks. A total-field/scattered-field source was used to separate the scattered field from the incident field, and the power flowing through the box surrounding the nanodisk was recorded to obtain the scattering cross-sections. For the scattering calculations, the maximum mesh size in all the *x*, *y* and *z* directions was set to 4 nm, whereas for the *x*–*y* plane near-field distribution calculations, the maximum mesh size in the *x*–*y* plane was set either to 1 or 2 nm (for disks with radii 190 and 350 nm, respectively). The near-field distributions were calculated for a *z* value corresponding to the centre of the disk, that is, height/2. In all the simulations, the 3R-MoS_2 nanodisk was placed on top of the glass substrate.

SHG. The SHG calculations were carried out using COMSOL Multiphysics (version 6.0). The computational domain consisted of a larger disk divided into two parts—the upper air media and the lower glass substrate. The 3R-MoS_2 nanodisk (with a defined $\chi^{(2)}$ tensor; Fig. 1b) was illuminated by a plane wave at a fundamental wavelength in the first electromagnetic-waves domain. The corresponding nonlinear polarization (current density) terms in the second electromagnetic-waves domain served as a source of the double-frequency photons (λ_{SHG}). The total SHG intensity was integrated over the outer surface area of the power density flow at λ_{SHG}.

The $\chi^{(2)}$ polarizability tensor was calculated using the method and tools outlined elsewhere[55]. Briefly, we calculated the nonlinear optical response using the DFT open-source GPAW package (version 22.1.0) employing the ASE library to construct the atomic structure. The Perdew–Burke–Ernzerhof exchange–correlation functional was used. The Kohn–Sham orbitals were expanded using a plane-wave basis set with an energy cutoff of 500 eV. We used a 21 × 21 × 3 Monkhorst–Pack grid for the **k** mesh and a grid spacing of less than 0.2 Å. The number of empty bands included in the sum over bands was set to three times the number of occupied bands. We used the Fermi–Dirac occupation number smearing with a factor of 20 meV and lineshape broadening of 50 meV. Time-reversal symmetry was imposed to reduce the *k* integrals to half.

Data availability

The data supporting the findings of this study are available within the Article and its Supplementary Information files, from the corresponding authors on reasonable request or via Zenodo at https://doi.org/10.5281/zenodo.10462850 (ref. 56).

References

55. Taghizadeh, A., Thygesen, K. S. & Pedersen, T. G. Two-dimensional materials with giant optical nonlinearities near the theoretical upper limit. *ACS Nano* **14**, 7155–7167 (2021).
56. Antosiewicz, T. J. & Zograf, G. Data and code for 'Combining ultrahigh index with exceptional nonlinearity in resonant transition metal dichalcogenide nanodisks'. *Zenodo* https://doi.org/10.5281/zenodo.10462850 (2024).

Acknowledgements

G.Z., A.Y.P., B.K. and T.O.S. acknowledge funding from the Swedish Research Council (VR Miljö project, grant no. 2016-06059 and VR project grant no. 2017-04545), the Knut and Alice Wallenberg Foundation (grant no. 2019.0140), Chalmers Area of Advance Nano, 2D-TECH VINNOVA competence center (ref. 2019-00068) and Olle Engkvist foundation (grant no. 211-0063). M.B. and T.J.A. acknowledge support from the Polish National Science Center via project 2019/34/E/ST3/00359. This work was performed in part at Myfab Chalmers and at the Chalmers Material Analysis Laboratory. Calculations were partially done at the Interdisciplinary Centre for Mathematical and Computational Modelling, University of Warsaw (#GC84-51).

Author contributions

G.Z., B.K. and T.O.S. conceived the idea. G.Z. carried out the optical experiments with the help of B.K. A.Y.P. and B.K. fabricated the samples and performed their characterization by SEM and AFM. M.B., G.Z. and T.J.A. carried out the numerical calculations of the DF scattering of individual disks, their near-field distributions and the SHG signal. T.J.A. performed the DFT analysis of the $\chi^{(2)}$ tensor of 3R-MoS_2. G.Z., B.K. and T.O.S. wrote the manuscript with the help of all authors.

Funding

Open access funding provided by Chalmers University of Technology.

Competing interests

The authors declare no competing interests.

Additional information

Extended data is available for this paper at https://doi.org/10.1038/s41566-024-01444-9.

Supplementary information The online version contains supplementary material available at https://doi.org/10.1038/s41566-024-01444-9.

Correspondence and requests for materials should be addressed to George Zograf or Timur O. Shegai.

Peer review information *Nature Photonics* thanks Alexander Tartakovskii and the other, anonymous, reviewer(s) for their contribution to the peer review of this work.